IEEE Access
Multidisciplinary | Rapid Review | Open Access Journal

Received April 19, 2021, accepted May 14, 2021, date of publication May 20, 2021, date of current version May 28, 2021.

Digital Object Identifier 10.1109/ACCESS.2021.3082175

Single Image Dehazing of Road Scenes Using Spatially Adaptive Atmospheric Point Spread Function

MINSUB KIM, SOONYOUNG HONG, HAEGEUN LEE, AND MOON GI KANG
School of Electrical and Electronic Engineering, Yonsei University, Seoul 03722, South Korea

Corresponding author: Moon Gi Kang (mkang@yonsei.ac.kr)

This work was supported by the National Research Foundation of Korea (NRF) grant funded by the Korea Government (MSIT) (No. 2019R1A2C2002167).

ABSTRACT Image haze removal is essential in autonomous driving as the outdoor images captured during unfavorable weather conditions, such as haze or snow, are affected by poor visibility. Much research has been done to overcome image degradation such as low contrast and faded color due to haze. However, in the traditional model, a phenomenon is neglected that several particles simultaneously involved in light acquisition. To address this problem, we propose a novel single image dehazing method based on the spatially adaptive atmospheric point spread function (APSF). We developed a module that estimates the APSF to overcome the limitations of the spatially invariant APSF which used in existing dehazing algorithms. The key factor in the estimation is that road scenes with haze have different statistical characteristic from common hazy images in color and resolution. Furthermore, the APSF on the traffic signs or lights is estimated by generating superpixels to prevent halo artifacts around the sharp edges of the images. We adopted the total variation model as a regularization functional to reduce halo and unnatural artifacts that may occur during deconvolution. The haze-free images from the proposed method tested whether the proposed method can enhance the performance of vision algorithms for autonomous driving. The experimental results demonstrate that the proposed method outperforms state-of-the-art image dehazing methods enhancing the performance of the vision algorithms. Moreover, additional experiments demonstrated the effectiveness of the proposed method for quantitative and qualitative comparison with the state-of-the-art algorithms.

INDEX TERMS Haze removal, single image dehazing, atmospheric point spread function, multiple scattering model, road scenes, deconvolution.

I. INTRODUCTION

Image acquired in bad weather conditions such as haze, rain and dust may suffer from low visibility. Suspended aerosols interact with light passing through the air, causing absorption and scattering, in bad weather on hazy or foggy days. This interaction causes serious image degradation such as blurring effects, reduced contrast, and false colors. As vision based autonomous driving and other Advanced Driver Assistance Systems (ADAS) were developed, the low visibility from bad weather condition may cause false detection [1]. A simple example of the effect of haze on the results of the vision algorithm is shown in Fig. 1. Therefore, an effective haze removal algorithm is required to ensure the reliable function of outdoor vision systems.

Many studies have been conducted on the effect of haze on color images. Several methods based on multiple images or fusion of different images. Schechner *et al.* [2] used a polarized camera to capture multiple images of the same scene with different polarization angles and calculated the atmospheric light and scene depth to obtain a clear image. Liang *et al.* [3] proposed a dehazing algorithm that fuses infrared and visible images to improve the visual quality of hazy images. Ancuti and Ancuti [4] proposed a method that fuses two diffidently enhanced images from an original hazy image to perform contrast enhancement. Although these approaches achieve remarkable results, they require a minimum of two images or additional cameras that use different spectral ranges, limiting their applications.

The associate editor coordinating the review of this manuscript and approving it for publication was Tianhua Xu.

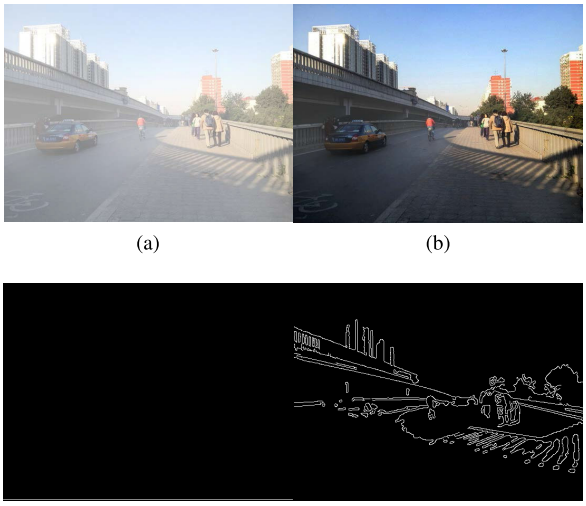

FIGURE 1. The effect of haze on image acquisition and edge detection. (a) hazy image, (b) result of the proposed method, (c) Canny edge detection of (a), and (d) Canny edge detection of (b).

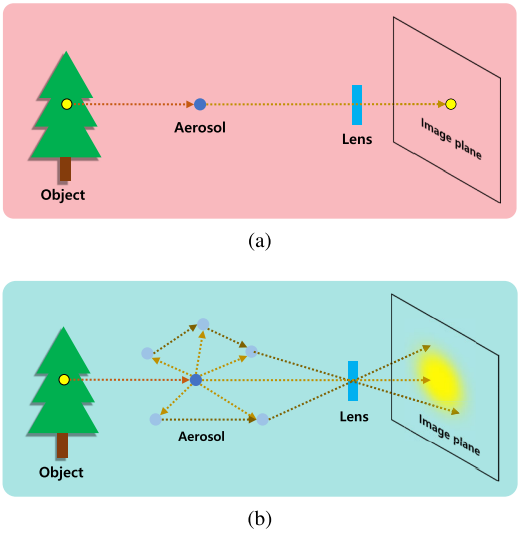

FIGURE 2. Image acquisition in an imaging system using (a) single scattering model and (b) multiple scattering model.

In recent years, single image dehazing methods have been extensively researched with significant advances that require priors or assumptions. Fattal [5] proposed a method to remove the effect of haze by estimating the albedo of the scene using the change of the color line. Zhu *et al.* [6] introduced a method based on the fact that haze decrease the color saturation and increases intensity. Tan [7] proposed an algorithm which based on the found that the haze-free image with fine visual effect presents relatively high contrast. Nishino *et al.* [8] introduced a Bayesian probability algorithm that jointly estimates the depth and scene albedo from a single image. Additionally, several image enhancement methods such as histogram equalization, wavelet transform, and Retinex methods exist [9].

Recently, convolutional neural network (CNN) have been applied in haze removal. Cai *et al.* [10] suggested that using trained receptive fields can produce results similar to heuristic priors, such as dark channel prior (DCP), indicating that neural networks can remove haze. This indicates that the neural network could be also used in haze removal. Ren *et al.* [11] proposed an effective multi-scale CNN to restore high quality haze-free images using the NYU depth dataset [12]. Li *et al.* [13] re-formulated an end-to-end dehazing CNN, AOD-Net, which can estimate transmission and atmospheric light simultaneously. Zhang and Patel [14] proposed the densely connected pyramid dehaze network that can examine scene depth and atmospheric light simultaneously. The hybrid approach to adapt exist dehazing method into learning based method also studied. Zhao *et al.* [15] adopted DCP to adversarial networks (GANs) to increase the visibility. Chen *et al.* [16] also used DCP for hybrid image learning. Although most image enhancement methods and deep-learning-based methods are easy to implement and some of them are based on the atmospheric scattering model, deep-learning-based models face certain challenges in training data. Furthermore, most of the existing studies use indoor image pairs for training and evaluate dehazing models. Owing to the lack of real-world hazy and clear image pairs, these learning based methods are ineffective in dealing with real-world haze images [15]. Moreover, as the suitable training data for the real-world road scene with haze is not enough, the learning-based methods may fail to remove the haze in the road scene.

On the other hand, many physics-based methods have also been proposed aimed at solving the inverse problem of the optical model to restore degraded images. Researchers have observed that the effects of aerosols such as Rayleigh scattering and Mie scattering follow the Koschmieder's law [17]. These effects on aerosols exponentially correlate with the depth of the scene. The widespread haze removal algorithms based on Koschmieder's law are single scattering model (SSM) which assumes only one particle affects the image acquisition. In SSM, the haze removal is an ill-posed problem as two unknown variables, scene depth and atmospheric light, exist in one equation.

This problem can be solved by setting a prior; the most commonly used prior is a DCP proposed by He *et al.* [18] wherein certain pixels with low intensities exist in at least one channel of RGB color space. Based on this prior, the distance between the object and the image acquisition device is estimated accurately to obtain a haze-free image. However, DCP fails to recover the sky regions in hazy images, owing to its similarity to the value of atmospheric light. Consequently, the color distortions appear in the restored images. Additionally, DCP sustains halo artifacts in depth discontinuities without time-consuming soft matting, as it assumes a constant depth in the local image patch. To address this problem, Li and Zheng [19] proposed to restore the haze image by exploiting globally guided image filter.

Furthermore, a non-local approach uses the change of pixel values to estimate the scene depth and atmospheric light,

FIGURE 3. Differences in applying deconvolution in dehazing. (a),(d) hazy image, (b),(c) dehazing with/without deconvolution using DCP, and (e),(f) dehazing with/without deconvolution using the proposed method.

as explained by Berman *et al.* [20]. Despite recent approaches based on the flexible adjust the level of the haze removal [21], boundary constraint [22], and etc., recover quality and complexity of the single image dehazing is still tough problem. Moreover, SSM ignores the atmospheric scattering with more than one particle despite adopting a physical model, which may cause blurring artifacts on the images [23].

Another approach to overcome this limitation of SSM is to use the multiple scattering model (MSM), which is based on the idea that more than one molecule affects the light acquired by the camera from an object in hazy conditions (Fig. 2). Unlike in SSM, light entering one pixel of a camera or image sensor in the MSM is affected by the surrounding region thus becoming blurred. Narasimhan and Nayar [24] defined a blur kernel for different weather conditions with the optical thickness defined as the atmospheric point spread function (APSF). Wang *et al.* [25] estimated the blur kernel using the generalized Gaussian distribution (GGD) to deblur the hazy image by means of a Wiener filter. The results of applying the SSM and the MSM to the same image are depicted in Fig. 3. The red box in Fig. 3 depicts that MSM restores the dense haze better than SSM. Using the blur kernel and deconvolution, high-frequency information reduced by the haze can be recovered, which can help estimate the transmission map for the dense haze regions as shown in Fig. 3. Thus, not only in the proposed method but also in the conventional dehazing method, the approach involving deconvolution is found to be helpful for haze removal.

As dehazing methods are based on the physical model, including image enhancement and deep-learning-based methods, they do not consider the characteristics of the road scene, resulting in darker regions and color shifts in road and traffic signs. Road regions with achromatic colors, such as asphalt, are affected by over-saturation or low visibility as haze removal methods make the roads darker. This causes low visibility in the region of interest, despite the removal of haze.

To address this problem, we propose a novel single image dehazing method with a spatially variant APSF for road scenes. We estimate a spatially variant blur kernel for haze removal to improve the visibility while reducing the artifacts caused by a spatially invariant blur kernel. Haze removal is achieved in two steps. Initially, we set the proper blur kernel with characteristics of haze in the road scene. We estimate the APSF using generalized normal distribution. Furthermore, the deblurred image is obtained, minimizing the artifacts at the edges. The second step estimates the remaining two unknown values, namely scene depth and atmospheric light, to recover the scene radiance.

We utilize the DCP proposed by He *et al.* [18] to estimate scene depth and atmospheric light. The dehazing method using DCP removes the haze effectively; however, it presents a disadvantage in images with dense haze. As the area affected by the haze more thicker, in terms of contrast the area have a lower dynamic range, also the low frequency component increases in terms of resolution. The low frequency and contrast complicate the estimation of transmission map in the haze removal method based on DCP, as all channels in the area have similar values. This problem can be overcome with deconvolution.

The novelty of our study is as follows:

- We propose how to estimate the blur kernel spatially variant with respect to the characteristics of the road scenes with haze.
- We adopt the superpixel algorithm for blur kernel and transmission estimations to consider the features of the road scenes, such as traffic signs and lights.
- We employ total variation (TV) as the regularization strategy to handle the edges and remove noise in the deconvolution process during haze removal.

The rest of this paper organized as follows. In section II, we review the conventional haze removal algorithms using MSM and explain the superpixel algorithm. Section III proposes a new haze removal algorithm with a spatially variant blur kernel for road scenes. In section IV, we evaluate the performance of the proposed method with application to several vision algorithms and analyze the subjective quality and objective metrics. Section V concludes the paper.

II. PROBLEM FORMULATION AND RELATED WORK

In this section, we present the existing SSM- and MSM-based image observation models for haze removal. Further, we define the spatially variant model for haze removal using image restoration theory. Finally the briefly review of the superpixel algorithm is presented.

A. HAZE REMOVAL USING MULTIPLE SCATTERING MODEL

In the SSM, the effect of haze can be defined as follows:

$$\mathbf{I} = \mathbf{J} \cdot \mathbf{t} + \mathbf{A}(1 - \mathbf{t}), \tag{1}$$

where $\mathbf{I}$ is the observed image, $\mathbf{J}$ is the scene radiance, $\mathbf{A}$ is the global atmospheric light, and $\mathbf{t}$ is the medium transmission.

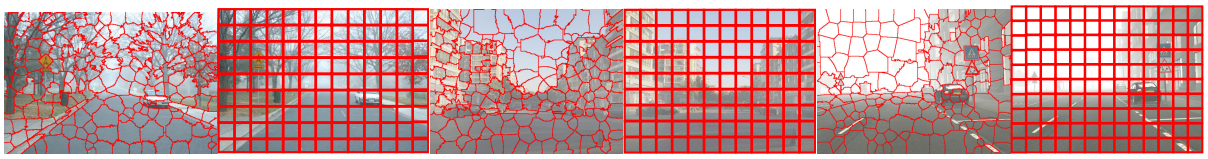

FIGURE 4. Difference in image segmentation between superpixels and patch-based method. (a), (c), (e) segmentation using superpixels; (b), (d), (f) segmentation using patch-based method.

t can be represented as

$$\mathbf{t} = \exp(-\eta \mathbf{d}), \tag{2}$$

where **d** is the depth and η denotes the atmospheric scattering coefficient.

However, in MSM, the effect of more than one particle results in an optical blur on the image plane, as illustrated in Fig. 2. Wei *et al.* [23] proposed that scene radiance can be blurred with the surrounding radiance. However, the method does not consider the optical blur caused by particles, and airlight. Narasimhan and Nayar [24] defined APSF which causes optical blur for isotropic point light source. The images obtained using MSM model can be expressed as:

$$\begin{aligned} \mathbf{I}_{blurred} &= \mathbf{I} * APSF \\ &= ((\mathbf{J} \cdot \mathbf{t} + \mathbf{A}(1 - \mathbf{t})) * APSF, \end{aligned} \tag{3}$$

where $*$ means convolution operation [26].

The modeling of the image degraded by the MSM is expressed as an ill-posed problem with three unknowns: *APSF*, **t**, and **A**, as shown in Eq. (3). Many studies have been conducted for accurate APSF estimation. The conventional methods used a single kernel based on the weather conditions, such as haze, fog, and rain as suggested by Narashiman *et al.* [24], and Wang *et al.* [25] used the GGD. Wang *et al.* substituted the shape and scale parameter values of GGD in a Legendre polynomial during application to several images. The Legendre polynomial requires one parameter value based on weather conditions; thus, the parameter value used by Wang *et al.* defines a spatially-invariant APSF for the entire image. However, spatially-invariant blur kernel generates artifacts in the flat areas and edges, as depicted in Fig. 6.

In image restoration theory, the input image degraded by the blur kernel can be mathematically modeled using the following equation:

$$\mathbf{y} = \mathbf{H}\mathbf{x} + \mathbf{n}, \tag{4}$$

where **y** is an observed image, **H** is the system matrix of degradation, **x** is the original image, and **n** is the corresponding error or noise, which assumed as Gaussian.

The artifact removal using APSF is considered as the image restoration problem, wherein **x** is determined as:

$$\mathbf{x} = \mathbf{I} = (\mathbf{J} \cdot \mathbf{t} + \mathbf{A}(1 - \mathbf{t})). \tag{5}$$

In the proposed method the degradation matrix **H** is estimated spatially variant to restore optical blur while suppress artifact and noise. Additionally, the system matrix **H** is estimated based on the characteristics of the road scenes, to solve the problem which road region goes darker with faded color. The spatially variant blur kernel can be mathematically modeled by the following equation:

$$\mathbf{y}_k = \mathbf{h}_k * \mathbf{x}_k + \mathbf{n}_k, \tag{6}$$

where k is the index for each region and $\mathbf{h}_k$ is the spatially variant blur kernel that is considered as APSF in this paper.

B. SUPERPIXEL ALGORITHM

A superpixel is a group of pixels sharing common characteristics, such as pixel intensity. The superpixel algorithm is widely used in the vision area because it can divides the entire image into a desired number of regions based on the characteristics of the region and provides useful primitives for evaluating the characteristics of local images [27]. However, owing to the calculation time and computational cost, the superpixels undergo image segmentation. Achanta *et al.* [27] calculated superpixels by simple linear iterative clustering (SLIC), which uses a 5-D space with the L^*, a^* and b^* values of the CIELAB color space and the x, y pixel coordinates for local clustering. Several approaches have been proposed using image segmentation with SLIC [9], [25], [28], [29]. The superpixel is used for segmentation of the sky region using object [25] or initial transmission estimation [25], [28], [29].

A road scene contains many objects, including traffic signs and lights. In traditional patch-based methods, these objects are affected by halo artifacts as the transmission map is estimated differently when the same object is split into multiple patches. Most conventional methods have different faded colors or halos appearing in one object, particularly where color information is essential. This problem can also occur in the deconvolution of artifacts, such as ringing artifacts and noise boosting, as incorrect kernel estimation of light sources. Therefore, blur kernel estimation and haze removal through segmentation for characteristic regions are required in a road scene.

In the proposed method, superpixels are used to estimate the APSF considering the characteristics of each region, and the regions are classified using the superpixel algorithm instead of the conventional patch-based algorithm. The proposed algorithm involves images containing haze in a road scene, and there may be cases wherein the same object is estimated as different transmission maps. The superpixel

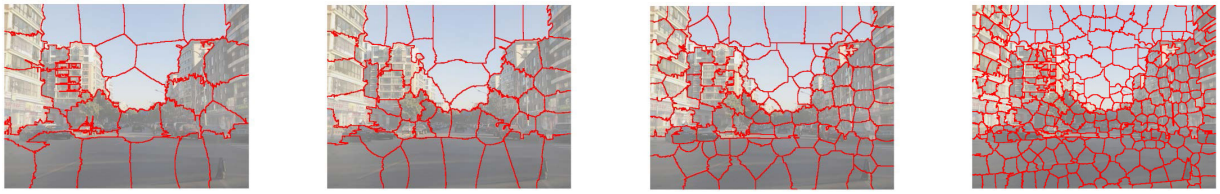

(a) (b) (c) (d)

FIGURE 5. Change in the segmented region according to the number of superpixels. (a) n = 30; (b) n = 50; (c) n = 100; (d) n = 300.

(a) (b)

FIGURE 6. Haze-removed image with deconvolution. (a) hazy image and (b) haze-removed image with the ringing artifact.

algorithm facilitates kernel estimation considering the characteristics of the region, using the cars, roads, and telephone poles as individual areas, as presented in Fig. 4. Conventional methods use superpixels to estimate and correct only the sky regions [25], whereas the proposed method uses superpixels in the main objects of the road regions as well. The difference in grouping of images according to the change in the number of superpixels in Fig. 5. Despite the increase in the number of groupings, the road and sky regions, the border between the building and sky, and the border between the building and road are divided into different groups.

III. PROPOSED METHOD

In this paper, we propose a single image haze removal algorithm using spatially variant APSF based on a MSM. The proposed algorithm is divided into three parts. At first, we set priors using the features of the road scene and calculate the APSF of each region. After estimating the blur kernel, the total variation is used to restore the degraded image while preserving the edge. This is followed by the estimation of the transmission map and airlight based on the deblurred image. Finally, the haze-removed image is obtained through the pixel-based blending method.

A. APSF ESTIMATION USING SUPERPIXEL ALGORITHM

In this section, the spatially adaptive APSF is estimated by measuring the effect of haze on each region. As mentioned earlier, applying the same kernel to the entire image generates various artifacts in regions that are less affected by the haze.

In the proposed method, the angle norm factor and gradient are set to model the characteristics of the road image; APSF for each region is defined using these two factors. Most road images are composed of a large amount of edge information (the peripheral portion excluding the road) and a flat area (road, vehicle bonnet, etc.). When the image is affected by haze, the overall contrast of the image including the edge information decreases. Choi *et al.* [30] measured the density of haze features such as contrast energy and image entropy. In our previous study [31], we measured the degree of haze contained in a region using the standard deviation and estimated the APSF of the region proportional to it. However, contrast alone cannot identify whether the area in which the kernel is estimated is an area with information not visible owing to the haze or a flat area without haze. Therefore, the proposed method estimates the blur kernel using the color information of the area segmented by superpixels combined with the gradient information.

Fig. 7 expresses the road image including haze and the value of each pixel in the RGB three-dimensional (3D) space. In the case of a haze-free image, pixels are evenly distributed in the R, G, and B planes, as depicted in Figs. 7(j)-(l). However, the distribution of the pixel values in hazy images containing details such as leaves, trees, and signs (Figs. 7(g)-(i)) indicates that the width is narrower than that of the haze-free image, although the distribution of the entire hazy image is not particularly focused on one side. If each pixel of the image is projected onto the RGB color space in this manner, a unique vector pointed by each pixel is obtained. This vector can be expressed as;

$$\mathbf{C}_i = [\mathbf{r}_i, \mathbf{g}_i, \mathbf{b}_i], \tag{7}$$

where i is the pixel position, $\mathbf{r}$, $\mathbf{g}$, and $\mathbf{b}$ are the vectors composed of the pixel value at each color channel.

Earlier studies have established that the distribution of images containing haze is concentrated around the achromatic series [1, 1, 1] in vector form with normalization between 0 and 1. The sky and the road regions expressed in the RGB color space in Fig 7. The distribution of the sky region (Figs. 7(a)-(c)) occupies a very narrow area in 3D space with most of the pointing vectors point in similar directions. This is regarded as having a similar direction vector (position vector) when each point in the sky area is considered as one vector. The road area (Figs. 7(d)–(f)) also exhibits a similar distribution (having one position vector),

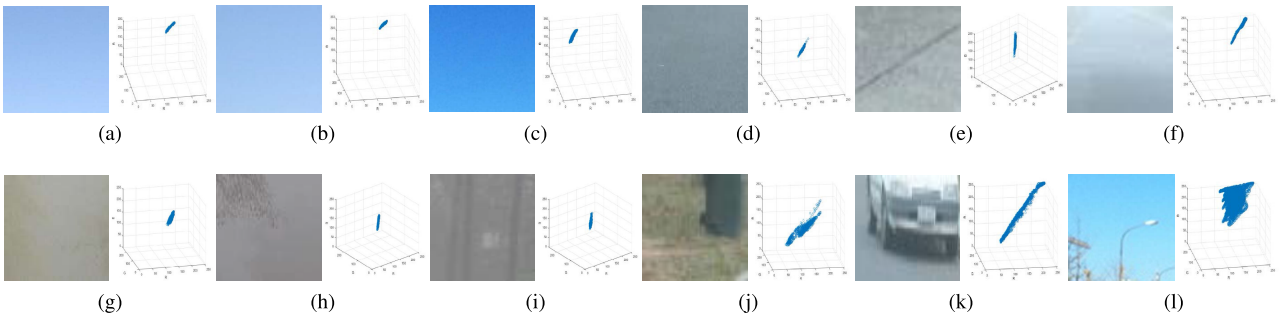

FIGURE 7. Expressing each pixel in RGB color domain for different patches. (a)–(c) sky area; (d)–(f) road area; (g)–(i) hazy area; (j)–(l) area without haze.

TABLE 1. Angle norm factor and the gradient value for Fig. 7.

	Fig. 7(a)	Fig. 7(b)	Fig. 7(c)	Fig. 7(d)	Fig. 7(e)	Fig. 7(f)	Fig. 7(g)	Fig. 7(h)	Fig. 7(i)	Fig. 7(j)	Fig. 7(k)	Fig. 7(l)
AF	0.013	0.011	0.242	0.004	0.004	0.012	0.015	0.026	0.026	0.047	0.018	0.050
Grad	0.255	0.173	0.701	1.264	1.637	0.920	0.682	3.202	5.883	3.074	12.919	4.517

with the vectors pointing in directions over a relatively wide range, which can be considered as a large vector magnitude. However, classifying an area using only a position vector has certain limitations. For example, although the distribution of the images in Figs. 7(j) and (k) have similar position vectors in the sky and the road areas, the vector is stretched more widely in Fig. 7(k). To define angle norm factor, first the average of the projected vectors is defined as a mean pointing vector, and the average of the angles formed by each vector with mean pointing vector is obtained. The angle norm factor can be expressed as;

$$AF_k = \frac{1}{n}\sum_{i\in N} \arccos\left(\frac{\mathbf{x}_i \cdot \boldsymbol{\mu}_k}{||\mathbf{x}_i||||\boldsymbol{\mu}_k||}\right), \tag{8}$$

$$\boldsymbol{\mu}_k = \frac{1}{n}\sum_{i\in N} \mathbf{C}_i = [\mu_{(r,i)}, \mu_{(g,i)}, \mu_{(b,i)}], \tag{9}$$

where μ is the mean of each color channel, k is the index of the separated group with superpixel algorithm, N is kth subset, and n is the number of the pixels in each subset N. Thus, the degree of haze through the distribution within a group in a color space is estimated using the angle norm factor.

The calculated gradient values and angle norm factors of the hazy, road, and sky areas are listed in Table 1. Although both the hazy and road areas have low angle norm factors, the value is lower in the road area than the dense hazy area. This is because when there are no unique parts such as a lane or a crack, the road area appears as a color composed of components of similar material. If the kernel is estimated with only the angle norm factor, artifacts occur in the road area as presented in Fig. 6.

To prevent this, the proposed method uses the gradient of each group to estimate the kernel. The effect of the haze appears low in the gradient because the haze component is applied as an additive term. Generally, the gradient value is small only in the area affected by the haze. However, in the image containing the haze, the sky region also has a small gradient value. The aforementioned color distribution appears in the road region as well; however, it has a larger value than the dense hazy region in terms of gradient. This is because the road surface has a rough surface and not perfectly flat owing to the different components (concrete, cement, stone, etc.). In the proposed method, the two regions, sky and road regions, are separated through a gradient.

The number of gradients in the region is defined as follows:

$$\begin{aligned} Grad_k(\mathbf{x}) &= ||\nabla \mathbf{x}||_1 = \sum_{i\in N} |\nabla x_i| \\ &= \sum_{i\in N} |\nabla_v x_i| + \sum_{i\in N} |\nabla_h x_i|, \end{aligned} \tag{10}$$

where $|\nabla_v x_i|$, and $|\nabla_h x_i|$ denote the vertical and horizontal differences between the adjacent pixels, respectively. Eq. (10) can determine the distribution in the edge of the area in more detail than the existing contrast measurement methods using variance and standard deviation.

The road region contains multiple areas with a small number of gradients, such as signs and lanes. These areas do not exhibit a significant distinction in the number of gradients before and after being affected by the haze. Consequently, it is difficult to determine the degree of haze using only the number of simple gradients. Therefore, the proposed method uses the color distribution of the area containing the haze to estimate the APSF kernel, compensating for the disadvantages of the two terms, the angle norm factor and gradient value.

In the proposed method, we utilizes the generalized normal distribution, wherein the additional parameters are added to the normal distribution, along with the two terms obtained to estimate the spatially variant APSF. The probability density function (PDF) of the normal distribution (Gaussian distribution) and the generalized normal distribution can be expressed

as follows:

$$f(z)_{normal} = \frac{1}{\sigma\sqrt{2\pi}} \exp\{-\frac{1}{2}(\frac{z-\psi}{\sigma})^2\}, \quad (11)$$

$$f(z)_{G\_normal} = \frac{\beta}{2\alpha\Gamma(1/\beta)} \exp(-\frac{|z-\psi|^\beta}{\alpha}), \quad (12)$$

where ψ is mean or location, σ is standard deviation and Γ is the gamma function. In a generalized normal distribution, the shape of the symmetric distribution is decided by the shape parameter β, which also has a relationship with kurtosis.

Kurtosis measures the 'tailedness' of the probability distribution of a real-valued random variable. The kurtosis is defined as follows:

$$Kurt[X] = E[(\frac{X-\psi}{\sigma})]^4 = \frac{\psi^4}{\sigma^4}. \quad (13)$$

For the generalized normal distribution, the kurtosis defined as:

$$Kurt = \frac{\Gamma(\frac{5}{\beta})\Gamma(\frac{1}{\beta})}{\Gamma(\frac{3}{\beta})^2}. \quad (14)$$

When kurtosis increases, the distribution is sharply pointed in the middle and decays slowly in the tails; when it decreases, the distribution becomes flatter on the top and thinner in the tails. In Figs. 8(b) and (c), the graph of lower kurtosis with sharp peak indicates the value of surrounding pixels. Thus, kurtosis defines the shape parameter because the lower and higher kurtosis increases and decreases the influence of the surrounding pixels, respectively.

In the proposed method, to improve the amount of information in the area with a high influence of haze, the APSF is set using the wide tail considering the surrounding area. The estimated wide tail kernel and deconvolution improves the amount of information before transmission map estimation. In addition, in areas where artifacts may occur because of deconvolution, such as road and sign areas, a kernel flattened from the top is estimated using a narrow tail.

Fig. 8(a) presents the relationship between kurtosis and the shape parameter, β. The change in β for each region region changes the kurtosis, determining the kernel shape. As the value of β decreases, kurtosis increases, and the PDF of the generalized normal distribution is estimated as a kernel of a shape considering the surrounding area, as the top portion becomes sharp and the tail portion becomes heavy. As the value of β increases, kurtosis decreases, and the PDF flattens the top area and is lighter at the tail, thus being estimated as a kernel that prevents ringing or other artifacts.

In the generalized normal distribution, the scale parameter α, determines the spread out degree of the probability distribution. As indicated in Fig. 8, the distribution changes according to α despite the same value of β. Therefore, calculating the value of α is equally important as that of β in determining the kernel. Figs. 8(b)–(e) present the different APSF kernels estimated based on the changes in α and β.

The proposed method estimates the different values of β for each region using the angle norm factor and the gradient value. If the angle norm factor is small owing to the color information in a region distributed in a similar direction, the influence of haze is considered significant. Therefore, a kernel capable of compensating for high-frequency information using the surrounding information before transmission map estimation is required. For regions with a low angle norm factor, a kernel with a sharp top region and a wide tail is used. Therefore, the angle norm factor and β are directly proportional, and β is expressed as follows:

$$\beta_k = c_1 \cdot AF_k, \quad (15)$$

where c_1 is the optimization parameter.

As mentioned previously, the gradient information distinguishes between areas containing a lot of haze that cannot be separated only by color distribution. Therefore, for regions with similar angle norm factors, smaller and larger gradient values result in the greater and lesser effect of haze, respectively. As the effect of haze increases, more information must be restored using a kernel with a wide tail. Thus, the gradient value is also proportional to β, wherein β is expressed as follows:

$$\beta_k = c_2 \cdot Grad_k, \quad (16)$$

where c_2 is the optimization parameter.

In the proposed method, the value α is set using the modified angle norm factor. As mentioned earlier, the angle norm factor indicates the degree of color distribution of a group. Although the width of the color distribution range of the group can be determined using the angle norm factor, it is difficult to ascertain whether the range indicates a specific color direction. For example, in the case of a sign composed of the same color, the saturation increases in the original color direction despite including the haze. These phenomena are often observed in road images, including traffic lights (red, green, and yellow), the color of the bonnet, and the headlights of vehicles coming from the opposite direction. The modified angle norm factor measures the angle between the color distribution of the group and the achromatic color. The change in the achromatic color increases when the general area is affected by the haze. Therefore, the pointing vector $[1, 1, 1]$ of $[R, G, B]$ in the 3D color space is used as the pointing vector of the achromatic color. The modified angle norm factor can be expressed as:

$$MAF_k = \frac{1}{n}\sum_{i\in n} \arccos(\frac{\mathbf{x}_i \cdot \mathbf{e}_p}{||\mathbf{x}_i||||\mathbf{e}_p||}),$$
$$\mathbf{e}_p = [1, 1, 1]. \quad (17)$$

In the case of the modified angle norm factor, a smaller angle between each vector and the achromatic pointing vector points in an achromatic direction. Therefore, information from the surrounding area must be utilized through a widespread kernel. However, in the case of signs and traffic lights, although the color distribution of the group is highly

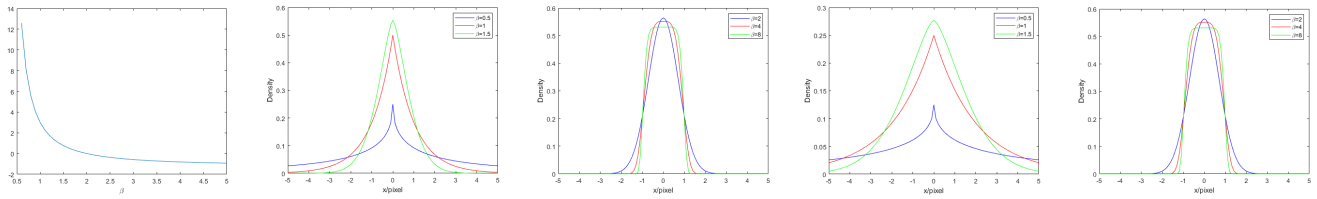

FIGURE 8. Kurtosis of generalized normal distribution and atmospheric point spread function kernel with different α and β (a) changes of the kurtosis with different β; (b), (c) $\alpha = 1$; (d), (e) $\alpha = 2$.

dense, the angle formed by the achromatic pointing vector increases owing to the distribution pointing toward the primary color in the color space. In that case, it is necessary to prevent aliasing through a narrow tail. Therefore, α and the modified angle norm factor are inversely proportional to each other, expressed as follows:

$$\alpha_k = \frac{c_3}{MAF_k}, \tag{18}$$

where c_3 is the optimization parameter. This relationship can be applied to gradient values as well; the regions with small gradient values have areas with both low (sky region) and high modified angle norm factors (traffic signs). Finally, the APSF for the each group k is estimated into:

$$APSF_k = \frac{\beta}{2\alpha\Gamma(1/\beta)} \exp(-\frac{|z-\psi|^\beta}{\alpha}), \tag{19}$$

where $\alpha = c_3/MAF_k$, and $\beta = c_1 \cdot c_2 \cdot AF_k \cdot Grad_k$.

Using Eq. (4) with $\mathbf{H}$ defined based on Eq. (19), $\hat{\mathbf{x}}$ can be restored through a process called deconvolution. Several deconvolution methods, such as Wiener filtering, Lucy–Richardson [32], [33], alternating direction methods of multipliers (ADMM) [34], [35] exist. As indicated in in Fig. 3, although the noise component may not be included in a haze composite image using computer graphics, actual image acquisition involves both haze and noise components. Therefore, it is necessary to use a deconvolution method to suppress noise components while preserving the edge information. This can be achieved using TV regularization rather than only data fidelity. The deblurred image $\hat{\mathbf{x}}$ can be expressed as follows:

$$\hat{\mathbf{x}_k} = \arg\min_{\mathbf{x}} ||\mathbf{y}_k - \mathbf{h}_k * \mathbf{x}_k||_2^2 + \lambda||\nabla\mathbf{x}_k||_1^1, \tag{20}$$

where λ is the regularization parameter. The difference between the deconvolution methods is presented in Fig. 9. As deconvolution cannot remove haze itself, we compared the result using the proposed dehazing method. The APSF kernel is estimated equally for two images and the only difference is deconvolution method. The edge information of an object can be preserved during deconvolution using TV, which prevents artifacts in the red box of Fig. 9.

As the image is restored from the optical blur using ADMM to solve the TV regularization problem, only two unknown values remain, which are estimated in the subsequent sections.

FIGURE 9. Difference in deconvolution methods indicating dehazing result using (a) Lucy–Richardson and (b) alternating direction methods of multipliers.

B. ESTIMATION OF TRANSMISSION MAP & AIRLIGHT

We estimated APSF and restored $\mathbf{x}$ into $\hat{\mathbf{x}}$ in section III-A. The two remaining unknown values are transmission map and atmospheric light.

The proposed method utilizes DCP. The transmission map is estimated using the deconvolved image with the estimated APSF. The DCP utilizes the prior that the lowest pixel value of the three channels in the region is 0 to solve the ill-posed problem. It can be expressed as follows:

$$J_{patch}^{dark}(p) = \min_{(k,l)\in\Omega} \min(J^c(k,l)), \tag{21}$$

where p is the dark channel value, k and l are pixel location, Ω is a local patch in general and c denotes color channels in color image which $c \in (r, g, b)$. Using DCP, the transmission map is estimated as follows:

$$\bar{t}_{patch}(k,l) = 1 - w \cdot \min_{(k,l)\in\Omega} \min_c (\frac{I^c(k,l)}{A^c}), \tag{22}$$

where $\bar{t}$ is estimated depth at (k, l) and w is adaptive parameter set to 0.95. The estimated transmission is called coarse transmission. If coarse transmission used with initial estimation, blocking artifacts occur at the boundary of each block. He *et al.* used a soft matting method to remove blocking artifacts. However, soft matting requires a lot of computation and time. Bilateral filtering [36] and guided filtering [37] has adopted to compensate computation while removing the artifacts. Also, by developing the single-scale, which uses one patch size entire image, methods based on multi-scale retinex method of utilizing multiple patch sizes such as small, medium, and large sizes and weighted summation were also developed [38]. Multi-scale methods prevent large objects

from being included in different patches. However, when the edge information of the image or the characteristics of the region are not known, this approach has a limit for dividing the scale.

In the proposed method, in order to compensate the limitations of the patch based DCP, transmission estimation of the segmented region through superpixel algorithm is used together. The method to obtain haze-free image through the two methods is described in section III-C. The DCP using superpixel is expressed as follows:

$$J^{dark}_{superpixel}(p) = \min_{(k,l)\in\Omega'} \min(J^c(k,l)), \tag{23}$$

where Ω' is the segmented group with superpixel algorithm, not a local patch. The transmission map is estimated as follows:

$$\bar{t}_{sp}(k,l) = 1 - w \cdot \min_{(k,l)\in\Omega'} \min_c (\frac{I^c(k,l)}{A^c}). \tag{24}$$

Since segmentation through superpixel algorithm is performed, the possibility of blocking artifacts that may occur in coarse estimation may also be less as the total number of masks is smaller than the method using the local patch. However, the boundary part divided by the superpixel algorithm is not shaped square in most cases (Fig. 5), and the size between the boundary is strong. Therefore, smoothing of the edge part is essential like the patch-based method. To achieve this, the proposed method utilizes the luminance information of the input image. The filtered transmission can be represented as follows:

$$\begin{aligned} tp_j &= ap_r L_j + bp_r, \\ tsp_j &= asp_r L_j + bsp_r, \end{aligned} \tag{25}$$

where tp and tsp are the filtered transmission for $\bar{t}_{patch}$ and $\bar{t}_{sp}$, respectively, and L denotes luminance component of the hazy image. The coefficients for guide filter can be expressed as:

$$\begin{aligned} a_r &= \frac{\frac{1}{|\Omega|}\sum_{i\in\Omega_r} L_i p_i - \mu_r \bar{p}_r}{\sigma_r^2 + \epsilon}, \\ b_r &= \bar{p}_r - a_r \mu_r, \end{aligned} \tag{26}$$

where p is $\bar{t}_{patch}$ for tp, and $\bar{t}_{sp}$ for tsp. The estimated transmission maps with two different approaches and the filtered transmission maps are presented in Fig. 10. The red box in Fig. 10(c) indicates that the estimation using superpixel easily identifies the signs on the road, whereas the patch-based estimation does not detect it. This can suppress halo artifacts during the dehazing process.

The final unknown value is atmospheric light. From the Koschmieder's law, the atmospheric light can be estimated where the scene depth is becomes 0. He *et al.* first picked 0.1% highest pixels from dark channel image, and estimate A as the highest value among those pixels. However, this poses a computation problem as all the pixels in the image must be sorted to pick the highest pixels.

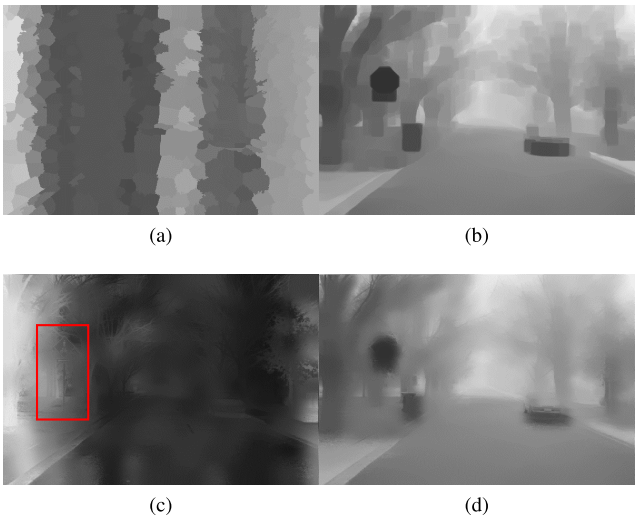

FIGURE 10. Estimated and filtered transmission maps of Fig. 3(d). (a) $\bar{t}_{sp}$; (b) $\bar{t}_{patch}$; (c) guided filtered $\bar{t}_{sp}$; (d) guided filtered $\bar{t}_{patch}$.

In the road scene, the sky region is generally included in the image, except in special cases, and is chiefly distributed on the upper side in the horizontal direction while the distribution in the vertical direction can vary. In the proposed method, to speed up the calculation time, the input image down-sampled 1/4 for horizontal and vertical direction. As the sky-region occupies most of the road scenes, the down sampling does not affect to the estimation of A.

We have to extract the object which has white values like streetlight while extracting the candidate pixels of A. Since the estimation of A is made for the pixel with the largest value, there is a possibility that the value of a white object such as a streetlight is estimated as the A value. In order to eliminate not only this possibility but also the problem of color noise, in the proposed method, morphological filtering is performed on the candidate set. Through this process, the influence of the sky region on the estimation of a value can be increased and the influence of small objects and edges can be reduced.

The haze-free image J can be restored using the deconvolved input I, A, and filtered transmission map. The haze-free image, scene radiance, is expressed as:

$$\begin{aligned} J_{patch}(k,l) &= \frac{I_{deconv}(k,l) - A}{max(tp(k,l), t_0)} \\ J_{sp}(k,l) &= \frac{I_{deconv}(k,l) - A}{max(tsp(k,l), t_0)}), \end{aligned} \tag{27}$$

where t_0 is a typical value that prevents the denominator from reaching 0. As we indicated earlier, we get two scene radiance which uses patch based DCP, and superpixel segmentation based DCP.

C. FUSION FOR A HAZE-FREE IMAGE

As mentioned in III-B, we obtain two different scene radiance J_{patch} and J_{sp} from Eq. (27). When the same operation (e.g. gamma correction, histogram equalization, white balance) is performed into the entire image, the degradation of the hazy

image is not eliminated because the optical density of haze varies across the entire image [4]. Codruta *et al.* performed weight map and multi-scale fusion using Gaussian and Laplacian pyramids, differences in luminance, chrominance, and visual saliency between the haze-removed image and the original image. However, this multi-scale fusion method is for an image in which only one operation is processed when the haze is removed, thus limiting the performance improvement.

In the case of an image obtained for transmission using a superpixel, the major edge portion of the image can be well-preserved. However, as the same transmission value is assumed for an area larger than the patch-based method, the haze-free image may become darker. Therefore, in the proposed method, the haze-free image is finally obtained using two different approaches. The weight map for the fusion of two images can be calculated in pixel units using the three factors proposed in III-A.

The weight map can be calculated based on the change in the amount of haze before and after removal. This implies that better haze removal increases the number of gradients, the color distribution is more diverse, and the achromatic tendency influencing the haze is reduced. In addition, comparing the original image with the image after haze removal preserves the original value before and after haze removal for, particularly road parts with small gradient values, traffic lights, and signs containing one color. The weight map can be expressed as follows:

$$W(k,l) = \frac{f^{sp}(k,l)}{f^{sp}(k,l) + f^{patch}(k,l)},$$
$$f(k,l) = \frac{AF(k,l) \cdot Grad(k,l)}{MAF(k,l)}, \tag{28}$$

where f^{sp} and f^{patch} are the factors for the superpixel-based and the patch-based haze-removed images, respectively, as mentioned in Eq. (27). The patch size used was identical to the one used in transmission map calculation. Additionally, we used the segmentation information of the input image because the characteristics of a haze-free image are different from the input image, owing to the superpixel segmentation. To remove the blocking artifact caused by the superpixel segmentation, we filtered weight map with guide image, for which we used multiplication of the patch-based and segmented images. Fig. 11 presents two haze-free image and weight map with filtering.

The final haze-free image is obtained with:

$$J(k,l) = W(k,l) \cdot J_{sp}(k,l) + (1 - W) \cdot J_{patch}(k,l). \tag{29}$$

IV. EXPERIMENTAL RESULTS

In this section, we validate the performance of our proposed method using multiple hazy images. The hazy images used in the experiment are divided into synthetic and naturally hazy images with and without ground truth, respectively. We obtained the synthetic images from the Frida image database [1], [39], Virtual KITTI dataset [40], O-HAZE database [41] and RESIDE database [42]. Unlike the synthetic image, natural hazy images do not have ground truth images, but it is necessary to use the natural hazy images to check whether the proposed method is applicable. For the natural hazy images, we collected various images using Flickr.com and several image search engines including hazy images from the paper Choi *et al.* proposed [30]. As the proposed method tests haze removal from road scenes, the experiment was conducted using only the images containing the road area and cars from the image databases.

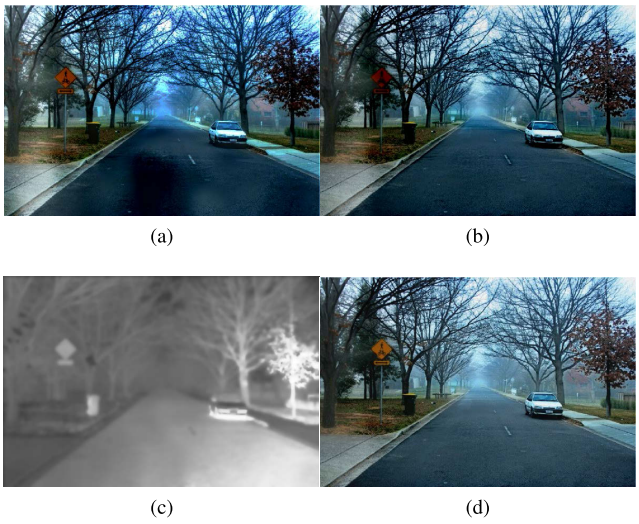

FIGURE 11. Haze-free images obtained using (a) superpixel algorithm, (b) patch-based algorithm. (c) weight map for fusion, and (d) haze-free image with fusion.

Initially, we compared the haze-removed images obtained using conventional methods. As the proposed method utilizes DCP, the algorithm proposed by He *et al.* was compared with the proposed algorithm. In addition, we compared the method of removing haze using color attenuation prior (CAP) [5], and the density of fog assessment-based defogger (DEFADE) method which analyzes the effect of haze on the image through various features [30]. To reflect the recent research on haze removal through a deep-learning approach, we compared the results of the proposed method with that of the CNN-based dehazing algorithm, DehazeNet [10]. The results of AOD-Net [13], a learning-based dehazing method using a scattering model, was also compared together. Additionally, the results of patch map based hybrid learning dehazeNet for single image haze removal (PMHLD) [16], which imported DCP into network, was compared to reflect recent research on haze removal. Finally, we compared our results with haze removal based on artificial exposure fusion (AMEF) [43] as it effectively removes haze from images using a one-sided histogram.

The results of the proposed method were compared with the conventional results from two perspectives. Initially, we applied the haze-removed image through each method to the vision algorithm that uses the road scene as the input image, verifying the effect of haze removal on the performance of vision algorithms: Vanishing point estimation

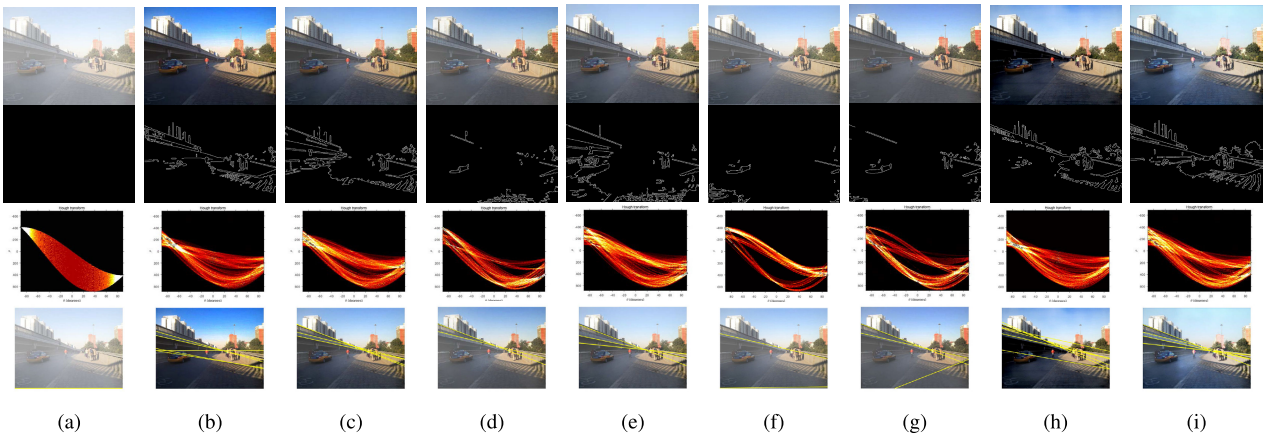

FIGURE 12. Comparison results of vision algorithms with different haze-removed methods. The first row is hazy and hazy-free images. The second row is edge map detected with Canny edge detector. The third row is the Hough transform for each results. The fourth row is detected vanishing point for each image. (a) the hazy image, (b) results of DCP, (c) results of CAP, (d) results of DEFADE, (e) results of DehazeNet, (f) results of AOD-Net, (g) results of AMEF, (h) results of PMHLD, (i) results of the proposed method.

utilizes the method proposed by Kong *et al.* [44] and line segment detector (LSD) proposed by Gioi *et al.* [45]. This is followed by a combined qualitative and quantitative comparisons of the results.

For the experiments, we set three parameters which estimates the APSF, c_1, c_2,and c_3 as 1, 1, and 10 respectively. The number of superpixels are set to 300 for each image. These parameters have been set up through various experiments.

A. APPLICATION AND EVALUATION FOR DRIVING ASSISTANCE SYSTEM

As the proposed method removes the haze effect in a road scene, a subjective evaluation of haze removal is essential to determine how the haze-removed image affects other applications while subjective evaluation of the removal of the effect of haze is also important. In this section, the performances of various vision algorithms are tested using road scenes to evaluate whether haze removal enhances their performance. We compare the results of the performance with the improvement of the Hough transform and edge detection using Canny edge detector, which is widely used in autonomous driving, and the results of the vanishing point estimation. Fig. 12 compares the result of the proposed method with the conventional methods.

As the Canny edge detector includes a threshold, the edge discrimination ability may vary depending on the threshold setting. In the Hough transform, thresholds are included in the parts that can be extracted as straight lines. We experimented without adjusting the threshold because calculating the optimal threshold for each image affects the detection.

Fig. 12(a), indicates that for a hazy image, the edge is not estimated using the Canny edge detector and the intersection of each line does not occur in the Hough transform. However, when the haze is removed using dehazing methods, the intersection between the deformed lines occurs through edge detection and Hough transform, validating that dehazing algorithms improve the performance of the vision algorithm. The edge information in the results of DEFADE, AMEF and AOD-net (Figs. 12(d), (g), and (f)) increases compared to the hazy image; however, the increase in edge information and the number of intersections in the Hough domain is smaller than those in other conventional algorithms, including the proposed method. The fourth row in Fig. 12 depicts the estimated vanishing point using Hough lines, indicated as yellow lines for each result. The vanishing point is estimated based on the intersection of the estimated Hough lines. The results of DCP and PMHLD (Figs. 12(b), and (h)) indicate that their ability to improve edge information is outstanding; however, as the Hough line is incorrectly estimated the vanishing point is estimated to be several points. Additionally, the two lines below are estimated to have no relation to the vanishing point. The results of CAP (Fig. 12(c)) adequately estimate the vanishing points through the intersection, while a limitation exists in estimating the Hough lines. The image in which the haze is removed using the proposed method (Fig. 12(i)) exhibits the best performance in estimating the amount of edge information and the vanishing point through the Hough line in comparison with the other methods, including DehazeNet (Fig. 12(e)). The metrics for the improvement in the amount of edge information are compared in Section IV-B.

The other widely used vision algorithm is line detection. Fig. 13 presents an image wherein haze is removed using the conventional algorithm, the hazy image, and the line estimated using LSD. The red box in Fig. 13(a) is a section with lanes that are important in autonomous driving. However, it is not considered as a line in an image containing haze. Although the results of DEFADE and AMEF(Figs. 13(d) and (g)), presents stable results for haze removal, but they cannot remove the haze effectively enough to detect a line in the red box. DCP (Fig. 13(b)) effectively removes haze while decreasing saturation, but does not effectively express the length of the lane depicted in red box. The other conventional

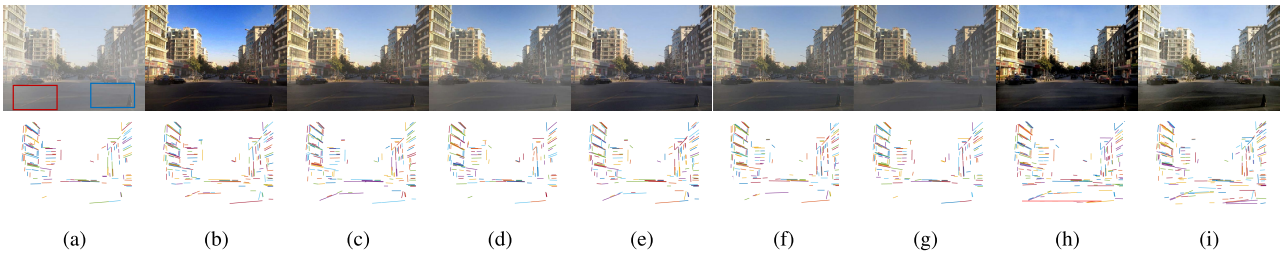

FIGURE 13. Comparison results of lane segment with different haze-removed methods. The first row is hazy and hazy-free images. The second row represents the detected line for each image. (a) the hazy image, (b) results of DCP, (c) results of CAP, (d) results of DEFADE, (e) results of DehazeNet, (f) results of AOD-Net, (g) results of AMEF, (h) results of PMHLD, (i) results of the proposed method.

methods, such as CAP, DehazeNet, AOD-Net and PMHLD (Figs. 13(c), (e), (f), and (h)) detect the line in the red box appropriately and express the edge information of the core depicted in the blue box properly. However, the proposed method (Fig. 13(i)) detects the lane in the red box and the edge information of the corners in the blue box, along with additional information such as other boundary parts, shadows, the boundary of the road, and the bottom of the vehicle, which can be utilized in the vision algorithms. Since the method proposed in the basic vision algorithm improves the detection performance of the algorithm, it can be applied to other vision algorithms.

B. SUBJECTIVE COMPARISON AND OBJECTIVE EVALUATION

To assess the performance of the proposed method, we tested various hazy images with images though conventional methods as mentioned in IV. For fair comparison, we set the patch size as 7×7 and lower bound t_0 as 0.1 for the patch-based methods, DCP, AMEF, and the proposed method. The patch size of the guided filter for the proposed method is set to 17×17 because it smoothened the blocking artifact reduction. The results of the conventional methods including proposed methods on the real-world images are on Fig. 14.

Although DCP removes haze sufficiently, there is no consideration for the sky or road areas, so artifacts such as noise amplification occur in the wide flat area like haze-opaque region. As indicated in the first row of Fig. 14(a), the dense haze in a distant place is not removed effectively. Additionally, the result of the DCP is over-saturated while removing the haze by using only one prior using the minimum channel, as depicted in fifth and sixth rows of Fig. 14(b).

The CAP algorithm, proposed by Zhu *et al.*, has weak ability to remove haze than DCP, while it removes haze better than DEFADE and DehazeNet. As the CAP algorithm based on the substitution of the brightness with increasing depth, the results images are unnatural or darker shown in first and fourth rows of the Fig. 14(c). Additionally, CAP removing the haze sufficiently in the anterior region of the image, the removal of relatively distant haze is limited, as depicted in the third and fourth rows of Fig. 14(c).

Although the DEFADE algorithm produces stable results, it does not eliminate the haze effects effectively. As indicated in Fig. 14(d), the haze in the anterior is removed sufficiently, but distant part retains some amount of haze. Additionally, the haze removal in the anterior is inferior compared to other algorithms because DEFADE initially calculates the density of haze with features. Although comfortable results are produced using these features, the drastic removal of haze is restricted.

In the case of deep-learning-based algorithm DehazeNet, the images become darker while removing the haze, as indicated in the third and fourth rows of Fig. 14(e). Additionally, DehazeNet has a limitation in restoring the haze located far from the image acquisition device (Fig. 14(e)), and the multiple scattering hazy images cannot be synthesized as DehzeNet examines only single scattering samples. This cause the result of the haze-removed image with blurring effect like fifth row of Fig. 14(e). The CNN for dehazing might be improved using the proposed method. And the other deep-learning-based algorithm, AOD-Net, shows stable results for the images which artificially generated in the last two rows of the Fig. 14. This is because most of the learning based algorithms are learned through a haze set made indoors. However, due to these characteristics, realness results cannot be produced for real world haze scenes that lack training data. As depicted in the first and the third rows of Fig 14(f), the learning-based methods removes less haze for the dense haze region or real world image than the prior-based methods including the proposed method.

This phenomenon also occurs in PMHLD, another learning-based algorithm. As indicated in the bottom three rows of Fig. 14(h), PMHLD yields better results than those of the other conventional methods for synthesized hazy images even when the road area is included. However, for a real-world hazy scene with the road area (top four rows of Fig. 14(h)), the performance is degraded in the dense haze area, and the road area becomes dark. This is because of the lack of training set for a real-world hazy scene with road area.

The final conventional method is AMEF which is based on the artificial exposure and image fusion. As AMEF is based on the fusion, it's results depends on the fusion fitting. As depicted in Fig. 14(g), although the AMEF provides stable results without halo artifacts, the result turns darker while removing haze (fifth row of Fig. 14(g)). Additionally, as the AMEF algorithm considers only the single scattering

FIGURE 14. Qualitative comparison of the different methods on real-world images. (a) the hazy image, (b) results of DCP, (c) results of CAP, (d) results of DEFADE, (e) results of DehazeNet, (f) results of AOD-Net, (g) results of AMEF, (h) results of PMHLD, (i) results of the proposed method.

model, it cannot remove the blurring effect caused by haze, as observed in the trees in the last row of Fig. 14(g).

The proposed method has the purpose of restoring the area with dense haze by using MSM and deconvolution. As indicated in the second row Fig. 14, the car that was not visible in the hazy image is clearly visible in the proposed method. In addition, the proposed method can also prevent dark regions from getting darker while removing the haze. The blue car on the left side of Fig. 14(i) proves that the dark area is better preserved compared to other algorithms. As the proposed method utilizes MSM, the blurring effect caused by haze can be removed during the dehazing process. Based on the fifth row of Fig. 14, the results obtained using the proposed method have a sharper edge for the cars on the road and the people in yellow clothes at the bus stop. This is observed in the last row of Fig. 14 for trees as well. Finally, the proposed method preserves the colors of materials such as asphalt and concrete of the road in the process of removing haze. Based on the first, third and fourth rows of Fig. 14, the color of the road is best preserved through CAP among conventional algorithms. DEFADE and DehazeNet have a limitation in removing haze in the road regions, while DCP and AMEF are over-saturated. However, the proposed method sets a prior for the road region using the gradient and the color component. Therefore, the result of Fig. 14(i) preserves and restores the road color despite the different materials.

The synthetic image validates the effectiveness of the proposed algorithm in removing the haze contained in the road compared to the conventional algorithms. Fig. 15 and Fig. 16 present synthetic images from the virtual KITTI, FRIDA, and FRIDA2 dataset created using computer graphics. These synthetic images are used for comparison of results because acquiring an image without haze and an image contained in the actual image under the same environment is difficult. For the virtual KITTI dataset, as indicated in Fig. 15(a), the cones behind the white sign are covered by haze, unlike in Fig. 15(j). Among the conventional methods, DCP and PMHLD (Figs. 15(b) and (h)), restore the cones. However, PMHLD does not remove haze at a distance. CAP and DEFADE (Figs. 15(a), and (d)) do not sufficiently remove the haze, whereas DehazeNet and AOD-Net (Figs. 15(e) and (f)) make the image darker. In contrast, the proposed method (Fig. 15(i)) restores the hazy image effectively while preserving the road regions and objects on the road, such as cars, signs, and the cones behind the sign. The FRIDA and FRIDA2 datasets contain four different haze types: homogeneous, heterogeneous and with and without cloud environments. Among the conventional methods, DCP yields the best performance in removing the four different types of haze. For the heterogeneous haze, most of the methods exhibited good performance in removing the haze; however, except for the proposed method, all other methods generated artifacts, indicated by color of the blue crosswalk sign changes in the

FIGURE 15. Qualitative comparison of the different methods on virtual KITTI image. (a) the hazy image, (b) results of DCP, (c) results of CAP, (d) results of DEFADE, (e) results of DehazeNet, (f) results of AOD-Net, (g) results of AMEF, (h) results of PMHLD, (i) results of the proposed method, (j) ground truth images.

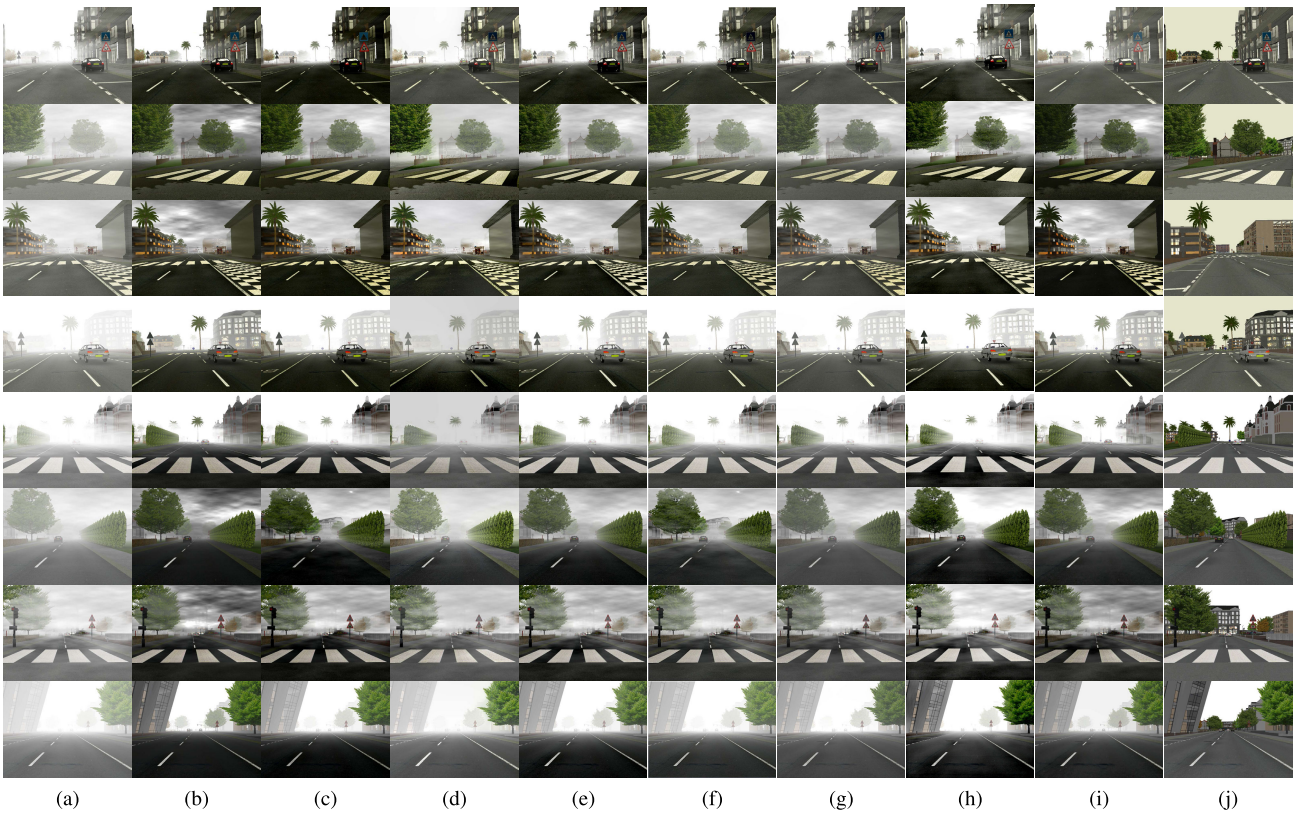

FIGURE 16. Qualitative comparison of the different methods on FRIDA and FRIDA2 data set image. First fifth rows: heterogeneous haze. Second sixth rows: cloudy homogeneous haze. Third seventh rows: cloudy heterogeneous haze. Fourth eighth rows: homogeneous haze. (a) the hazy image, (b) results of DCP, (c) results of CAP, (d) results of DEFADE, (e) results of DehazeNet, (f) results of AOD-Net, (g) results of AMEF, (h) results of PMHLD, (i) results of the proposed method, (j) ground truth images.

first row of Fig. 16. However, the proposed method removes the haze up to the location where the tree is visible without changing the color of objects, including signs. The deep-learning-based methods, DehazeNet and AOD-Net, make the road darker while removing haze. PMHLD exhibits the second best performance among the deep-learning-based algorithms; however, it is not as effective in dense haze areas with cloudy environments. The CAP algorithm, is based on the color change, causing the dehazed image to becomes darker and decreasing the saturation particularly in achromatic areas with objects such as cars and roads. Finally, the AMEF method removes haze without generating artifacts; however, it does not remove dense haze regions. The proposed method removes all four haze types without generating artifacts or causing a color change of the objects in the road scene.

Unlike real world data, synthetic data has the original image. Therefore, the amount of haze effect removed by the dehazing algorithms can be measured and compared to the original image. Table 2, presents the quantitative measurements for Fig. 15 and Fig. 16. For the virtual KITTI dataset, 150 images were selected and all images in FRIDA and FRIDA2 conducted in the experiment. Three metrics, namely structural similarity index (SSIM) [46], peak signal to noise ration (PSNR) and fog aware density evaluator (FADE), were used to compare the results of the proposed method with the conventional methods. SSIM is an image quality metric based on the computation of three terms, the luminance tern, the contrast term and the structural term. SSIM is an index that better expresses how similar the original and processed images are in the human visual system than the

TABLE 2. Quantitative measurement results of synthetic datasets.

Dataset	Metrics	hazy	DCP	CAP	DEFADE	DehazeNet	AOD-Net	AMEF	PMHLD	proposed
Virtual KITTI(150 samples)	SSIM	0.426	0.467	0.443	0.409	0.182	0.425	0.377	0.413	0.505
	PSNR	6.743	8.755	9.419	8.606	5.773	8.2241	8.750	0.732	8.829
	FADE	1.274	0.382	0.714	0.371	0.347	0.412	1.201	0.315	0.246
FRIDA(76 samples)	SSIM	0.616	0.600	0.522	0.566	0.614	0.629	0.680	0.563	0.693
	PSNR	11.167	13.316	12.494	13.226	12.926	13.229	14.456	12.697	13.875
	FADE	1.843	0.754	0.690	1.059	0.727	0.893	1.237	0.564	0.693
FRIDA2(264 samples)	SSIM	0.737	0.642	0.334	0.756	0.662	0.440	0.787	0.656	0.803
	PSNR	10.472	11.638	8.826	12.048	11.800	9.749	12.713	11.695	12.549
	FADE	2.783	1.158	0.628	1.952	0.974	1.081	1.860	0.732	0.801

PSNR calculated by simply calculating the mean square error between pixels. The SSIM has boundary between 0 and 1, the value near 1 means output image has similar structure with reference image. FADE is proposed by choi *et al.* which calculates the density of haze with features. The smaller value of FADE means the image contains less haze component. In Table 2, the numbers highlighted the darkest, second darkest, and third darkest denote the highest, second-highest, and third-highest performances, respectively.

In virtual KITTI dataset, the proposed method showed the highest and second-highest performances for SSIM and PSNR, respectively; the DCP and CAP presented the third-highest and the highest results for the SSIM and PSNR, respectively. As the SSIM calculates the structural similarity between the output image and reference image, the proposed method restores the hazy image effectively among conventional methods. This is also validated by the proposed method exhibiting the lowest FADE value, which measures the density of the haze, while the hazy image has the highest FADE value. In the FRIDA and FRIDA2 dataset, the proposed method shows at least the third highest for all metrics. This shows the proposed methods removes haze effectively with quantitative metrics.

To evaluate the performance of the proposed method quantitatively for natural images, several metrics measured the improvement of the hazy image. We focus on the image quality into four parts. As the natural images does not have images with haze, the metrics are almost blind quality measurements. Initially, we apply a blind assessment metric derived in [47], which measures the improvement by the ratios of the newly visible edges and gradient magnitudes. The newly visible edges and the ratio of the gradient norms over edges are denoted by the indicators e and $\bar{r}$, respectively. The larger values of e and $\bar{r}$ indicates a better restoration of haze. We adopted natural image quality evaluator (NIQE) [48] to measure whether the results distorted while dehazing. The NIQE indicator measures the quality of the image using the features from natural scene statistics (NSS). Low values of NIQE indicates that the output image has lower distortions and distributions similar to NSS. The indicator FADE is calculated using all the experimental images with various algorithms, as we chose FADE for changing the haze density. Finally, to measure the improvement of the dehazing algorithm, we apply the recently proposed indicator to the overall dehazing quality index (DHQI) [49]. DHQI calculates the overall dehazing quality of the algorithms with haze removing features, structure-preserving features, and over-enhancement features which are the key aspects of dehazing. High DHQI values indicate better restoration of the hazy image. Table 3 calculates the five assessment criteria for the images in Figs. 12 and 13. The numbers highlighted the darkest, second darkest, and third darkest denote the highest, second-highest, and third-highest performances, respectively, similar to Table 2.

Table 3 shows that in most cases, the proposed method exhibits the highest performance for all four haze types. While DCP presents the highest performance for e, PMHLD shows the best results among the conventional methods. This indicates that the DCP-based method and PMHLD perform better than other conventional methods in terms of new visible edges and haze density. However, Table 3 also validates that the results of the conventional methods exhibit lower quality in terms of NSS after dehazing, except for the proposed method. The PMHLD method exhibits the highest performance among the conventional methods for the DHQI index in Figs. 12 and 13. The proposed method exhibits the second highest performance in the overall quality measurements except $\bar{r}$. This indicates that the newer algorithms are performing better and the newer metrics may be suitable for recent algorithms. This result reveal that the proposed algorithm not only aids in improving the performance of the vision algorithm, but also demonstrates high dehazing performance quantitatively.

As presented in Table 4, the highest performance among dehazing methods depends on the input image. The image set in Fig. 14 is composed of the road scenes with different image acquisition angle, railroad scene, and sidewalk with people. DCP shows better performance for the new visible edges, with less haze density. However, DCP exhibits low quality with NIQE and DHQI, caused by the over-saturation and noise boosting at the sky region of the DCP. Despite CAP presents a stable result and high value in DHQI, it does

TABLE 3. Quantitative measurement results IN terms of e, $\bar{r}$, NIQE, FADE, DHQI, and SSIM on the Fig. 12 and Fig.13.

Image	Metrics	hazy	DCP	CAP	DEFADE	DehazeNet	AOD-Net	AMEF	PMHLD	proposed
Fig.12	e	-	1.959	1.706	0.915	1.152	1.139	0.850	1.918	1.762
	$\bar{r}$	-	1.723	1.768	1.810	1.751	2.048	1.587	2.225	1.799
	NIQE	2.303	2.713	2.537	2.380	2.345	2.564	2.469	2.324	2.266
	FADE	3.236	0.818	1.004	1.247	1.327	1.457	1.295	0.455	0.798
	DHQI	17.581	52.870	59.018	57.542	60.26	53.250	58.067	61.809	61.811
Fig.13	e	-	1.094	0.592	0.233	0.605	0.544	0.326	0.802	0.805
	$\bar{r}$	-	1.937	1.751	1.450	0.778	1.922	1.403	2.079	2.202
	NIQE	2.515	3.219	2.953	2.782	2.737	3.133	2.667	2.512	2.150
	FADE	2.464	0.580	0.953	1.206	0.965	1.088	1.142	0.314	0.813
	DHQI	49.861	59.160	61.686	58.987	63.554	50.318	60.643	67.052	67.136

TABLE 4. Quantitative measurement results IN terms of e, $\bar{r}$, NIQE, FADE, and DHQI on the Fig. 14.

Image	Metrics	hazy	DCP	CAP	DEFADE	DehazeNet	AOD-Net	AMEF	PMHLD	proposed
Fig.14 1st row	e	-	0.505	0.552	0.642	0.250	0.475	0.261	0.304	0.583
	$\bar{r}$	-	1.506	1.364	1.843	1.456	1.714	1.451	1.696	1.823
	NIQE	1.696	1.786	1.766	1.867	1.691	1.815	1.998	2.934	1.639
	FADE	0.962	0.318	0.260	0.241	0.293	0.400	0.425	0.311	0.221
	DHQI	56.779	69.312	69.023	69.505	68.898	67.858	68.764	69.035	69.510
Fig.14 3rd row	e	-	0.502	0.385	0.496	0.450	0.528	0.155	0.397	0.612
	$\bar{r}$	-	1.667	1.373	1.885	1.215	1.474	1.016	1.804	1.746
	NIQE	3.270	3.416	3.439	3.968	3.543	3.659	3.460	3.199	2.480
	FADE	1.074	0.393	0.591	0.194	0.232	0.368	0.883	0.448	0.300
	DHQI	57.765	65.839	63.462	64.589	68.482	55.686	61.697	63.692	65.793
Fig.14 4th row	e	-	1.126	1.293	0.936	1.125	0.985	0.422	1.025	0.827
	$\bar{r}$	-	1.600	1.021	1.844	1.345	1.470	1.036	2.361	1.497
	NIQE	3.202	2.746	3.080	2.691	2.992	3.256	3.220	2.890	2.684
	FADE	1.198	0.354	0.239	0.245	0.277	0.348	0.756	0.335	0.325
	DHQI	57.765	65.839	63.462	64.589	68.482	64.655	61.697	62.294	65.793
Fig.14 5th row	e	-	1.582	1.098	0.923	1.006	0.770	1.025	0.372	1.086
	$\bar{r}$	-	1.531	1.572	1.603	1.633	1.815	1.136	1.373	1.833
	NIQE	2.406	2.542	2.558	2.299	2.463	2.482	2.288	2.943	2.310
	FADE	3.063	0.819	1.202	1.512	1.291	1.342	1.722	0.672	1.095
	DHQI	49.416	51.726	59.273	58.234	58.645	49.443	56.159	60.620	61.208
Fig.14 6th row	e	-	0.519	0.428	0.219	0.332	0.876	0.222	1.291	0.776
	$\bar{r}$	–	1.472	1.149	1.372	1.418	1.970	1.189	2.065	1.855
	NIQE	2.339	2.559	2.448	2.426	2.435	2.840	2.566	2.685	2.186
	FADE	2.421	0.677	0.659	1.353	0.763	1.198	1.253	0.328	0.685
	DHQI	51.203	58.364	65.432	58.346	66.225	50.416	60.288	65.607	67.575
Fig.14 7th row	e	-	0.844	0.710	0.643	0.577	0.575	0.572	0.417	0.776
	$\bar{r}$	–	1.628	1.488	1.791	1.570	1.734	1.426	1.655	1.828
	NIQE	2.386	2.455	2.534	2.642	2.395	2.516	2.423	2.118	2.658
	FADE	1.291	0.417	0.399	0.523	0.503	0.551	0.616	0.486	0.362
	DHQI	53.121	68.799	70.730	66.472	69.174	67.113	68.061	68.136	71.976

not produce a higher result than other algorithms in the new visible edge. However, it performs better than other methods in scenes that include railroads. DEFADE performs the best among conventional methods, in which the visible edge increases, the NIQE does not increase compared to the hazy image, and the haze density decreases in real-world image.

TABLE 5. Quantitative measurement results IN terms of e, $\bar{r}$, NIQE, FADE, and DHQI on various image sets.

Metrics	hazy	DCP	CAP	DEFADE	DehazeNet	AOD-Net	AMEF	PMHLD	proposed
e	-	1.323	1.208	0.806	1.082	0.972	0.457	1.189	1.387
$\bar{r}$	-	1.548	1.392	1.719	1.527	1.845	1.201	1.840	1.856
NIQE	2.813	3.000	2.922	2.918	2.836	3.105	2.844	2.892	2.795
FADE	2.156	0.655	0.854	0.843	0.856	0.995	1.286	0.449	0.639
DHQI	51.012	55.443	61.668	59.264	62.959	52.014	58.453	60.862	63.085

However, it does not produce better performance than the proposed method because the restoration of the area where dense haze exists is low. Despite Dehazenet exhibiting high performance in DHQI, image darkening worsens the performance compared to other conventional methods in terms of the new visible edge and contrast. PMHLD exhibits a good performance for FADE and DHQI, but it has a limitation in dense haze removal. The metric for new visible edges is not high for PMHLD. Although AMEF does not generate artifact such as halo, the quantitative measurements of AMEF are not higher than those of the conventional methods. The proposed method demonstrates a better performance for images with haze acquired from the top view of the road and sidewalk with people. However, the proposed method has a lower quality index for the scene with a railroad because it has a prior with road scenes.

Finally, we select 150 haze images from dataset and real-world images mentioned in IV and restore all images using the conventional methods including the proposed methods. Table 5 shows the average of each quality metrics to measure the dehazing performance. Table 5 indicate that the proposed method outperforms the conventional methods in terms of new visible edge, blind image quality from NSS, density of haze, and the overall dehazing quality. The experimental results validate that the proposed method can be extended to general haze images as well as haze with road images.

V. CONCLUSION

In this paper, we propose a novel haze removal algorithm using a multiple scattering model. Unlike the most of the existing approaches are based on the single scattering model, or spatially invariant blur kernel, we proposed a spatially variant atmospheric point spread function with superpixel algorithm. Moreover, the generalized normal distribution is employed to model the physical blur kernel caused by multiple scattering, atmospheric point spread function. We define the blur kernel of each region with three different prior for characteristics of the road scenes: the angle norm factor, gradient value, and the modified angle norm factor. To prevent artifacts from edges and remove noise, the total variation regularization is adopted. Experimental results indicate that the proposed method can be applied to improve the performance of the vision based algorithm for road scenes. The proposed method evaluated using subjective assessment as well as objective measures. The comparison results indicates that the proposed method can achieve better results than the other state-of-the-art dehazing algorithms quantitatively and qualitatively.

REFERENCES

[1] J.-P. Tarel, N. Hautiere, L. Caraffa, A. Cord, H. Halmaoui, and D. Gruyer, "Vision enhancement in homogeneous and heterogeneous fog," *IEEE Intell. Transp. Syst. Mag.*, vol. 4, no. 2, pp. 6–20, 2012.

[2] Y. Y. Schechner, S. G. Narasimhan, and S. K. Nayar, "Polarization-based vision through haze," *Appl. Opt.*, vol. 42, no. 3, pp. 511–525, 2003.

[3] J. Liang, W. Zhang, L. Ren, H. Ju, and E. Qu, "Polarimetric dehazing method for visibility improvement based on visible and infrared image fusion," *Appl. Opt.*, vol. 55, no. 29, pp. 8221–8226, 2016.

[4] C. O. Ancuti and C. Ancuti, "Single image dehazing by multi-scale fusion," *IEEE Trans. Image Process.*, vol. 22, no. 8, pp. 3271–3282, Aug. 2013.

[5] R. Fattal, "Dehazing using color-lines," *ACM Trans. Graph.*, vol. 34, no. 1, pp. 1–14, Dec. 2014.

[6] Q. Zhu, J. Mai, and L. Shao, "A fast single image haze removal algorithm using color attenuation prior," *IEEE Trans. Image Process.*, vol. 24, no. 11, pp. 3522–3533, Nov. 2015.

[7] R. T. Tan, "Visibility in bad weather from a single image," in *Proc. IEEE Conf. Comput. Vis. Pattern Recognit.*, Jun. 2008, pp. 1–8.

[8] K. Nishino, L. Kratz, and S. Lombardi, "Bayesian defogging," *Int. J. Comput. Vis.*, vol. 98, no. 3, pp. 263–278, Jul. 2012.

[9] Y. Tan and G. Wang, "Image haze removal based on superpixels and Markov random field," *IEEE Access*, vol. 8, pp. 60728–60736, 2020.

[10] B. Cai, X. Xu, K. Jia, C. Qing, and D. Tao, "DehazeNet: An end-to-end system for single image haze removal," *IEEE Trans. Image Process.*, vol. 25, no. 11, pp. 5187–5198, Nov. 2016.

[11] W. Ren, S. Liu, H. Zhang, J. Pan, X. Cao, and M.-H. Yang, "Single image dehazing via multi-scale convolutional neural networks," in *Proc. Eur. Conf. Comput. Vis.* Cham, Switzerland: Springer, 2016, pp. 154–169.

[12] N. Silberman, D. Hoiem, P. Kohli, and R. Fergus, "Indoor segmentation and support inference from RGBD images," in *Eur. Conf. Comput. Vis.* Berlin, Germany: Springer, 2012, pp. 746–760.

[13] B. Li, X. Peng, Z. Wang, J. Xu, and D. Feng, "AOD-net: All-in-One dehazing network," in *Proc. IEEE Int. Conf. Comput. Vis. (ICCV)*, Oct. 2017, pp. 4770–4778.

[14] H. Zhang and V. M. Patel, "Densely connected pyramid dehazing network," in *Proc. IEEE/CVF Conf. Comput. Vis. Pattern Recognit.*, Jun. 2018, pp. 3194–3203.

[15] S. Zhao, L. Zhang, Y. Shen, and Y. Zhou, "RefineDNet: A weakly supervised refinement framework for single image dehazing," *IEEE Trans. Image Process.*, vol. 30, pp. 3391–3404, 2021.

[16] W.-T. Chen, H.-Y. Fang, J.-J. Ding, and S.-Y. Kuo, "PMHLD: Patch map-based hybrid learning DehazeNet for single image haze removal," *IEEE Trans. Image Process.*, vol. 29, pp. 6773–6788, 2020.

[17] H. Koschmieder, "Theorie der horizontalen sichtweite," *Beitrage zur Physik der freien Atmosphare*, pp. 33–53, 1924.

[18] K. He, J. Sun, and X. Tang, "Single image haze removal using dark channel prior," *IEEE Trans. Pattern Anal. Mach. Intell.*, vol. 33, no. 12, pp. 2341–2353, Dec. 2011.

[19] Z. Li and J. Zheng, "Single image de-hazing using globally guided image filtering," *IEEE Trans. Image Process.*, vol. 27, no. 1, pp. 442–450, Jan. 2018.

[20] D. Berman, T. Treibitz, and S. Avidan, "Non-local image dehazing," in *Proc. IEEE Conf. Comput. Vis. Pattern Recognit. (CVPR)*, Jun. 2016, pp. 1674–1682.

[21] Z. Ling, G. Fan, J. Gong, Y. Wang, and X. Lu, "Perception oriented transmission estimation for high quality image dehazing," *Neurocomputing*, vol. 224, pp. 82–95, Feb. 2017.
[22] S. Chan, P. Gill, and T. Nguyen, "An augmented Lagrangian method for total variation video restoration," *IEEE Trans. Image Process.*, vol. 20, no. 11, pp. 3097–3111, Nov. 2011.
[23] P. Wei, Y. Liu, Y. Liu, and S. Wang, "Dehazing model based on multiple scattering," in *Proc. 3rd Int. Congr. Image Signal Process.*, vol. 1, Oct. 2010, pp. 249–252.
[24] S. G. Narasimhan and S. K. Nayar, "Shedding light on the weather," in *Proc. IEEE Comput. Soc. Conf. Comput. Vis. Pattern Recognit.*, vol. 1, Jun. 2003, pp. I–I.
[25] R. Wang, R. Li, and H. Sun, "Haze removal based on multiple scattering model with superpixel algorithm," *Signal Process.*, vol. 127, pp. 24–36, Oct. 2016.
[26] S. Tao, H. Feng, Z. Xu, and Q. Li, "Image degradation and recovery based on multiple scattering in remote sensing and bad weather condition," *Opt. Exp.*, vol. 20, no. 15, pp. 16584–16595, 2012.
[27] R. Achanta, A. Shaji, K. Smith, A. Lucchi, P. Fua, and S. Süsstrunk, "Slic superpixels," EPFL, Tech. Rep. 1049300, 2010. [Online]. Available: http://infoscience.epfl.ch/record/149300
[28] M. Yang, Z. Li, and J. Liu, "Super-pixel based single image haze removal," in *Proc. Chin. Control Decis. Conf. (CCDC)*, May 2016, pp. 1965–1969.
[29] S.-W. Noh, B. Ahn, and I. S. Kweon, "Haze removal on superpixel domain," in *Proc. 10th Int. Conf. Ubiquitous Robots Ambient Intell. (URAI)*, Oct. 2013, pp. 597–598.
[30] L. Kwon Choi, J. You, and A. C. Bovik, "Referenceless prediction of perceptual fog density and perceptual image defogging," *IEEE Trans. Image Process.*, vol. 24, no. 11, pp. 3888–3901, Nov. 2015.
[31] M. Kim, S. Hong, and M. G. Kang, "Single image haze removal using multiple scattering model for road scenes," *Electron. Imag.*, vol. 2020, no. 16, pp. 1–81, 2020.
[32] L. B. Lucy, "An iterative technique for the rectification of observed distributions," *Astronomical J.*, vol. 79, p. 745, Jun. 1974.
[33] W. H. Richardson, "Bayesian-based iterative method of image restoration," *J. Opt. Soc. Amer.*, vol. 62, no. 1, pp. 55–59, Jan. 1972.
[34] Y. Wang, J. Yang, W. Yin, and Y. Zhang, "A new alternating minimization algorithm for total variation image reconstruction," *SIAM J. Imag. Sci.*, vol. 1, no. 3, pp. 248–272, Jan. 2008.
[35] B. Wahlberg, S. Boyd, M. Annergren, and Y. Wang, "An ADMM algorithm for a class of total variation regularized estimation problems," *IFAC Proc. Volumes*, vol. 45, no. 16, pp. 83–88, 2012.
[36] C. Xiao and J. Gan, "Fast image dehazing using guided joint bilateral filter," *Vis. Comput.*, vol. 28, nos. 6–8, pp. 713–721, Jun. 2012.
[37] J. Pang, O. C. Au, and Z. Guo, "Improved single image dehazing using guided filter," in *Proc. APSIPA ASC*, 2011, pp. 1–4.
[38] B. Xie, F. Guo, and Z. Cai, "Improved single image dehazing using dark channel prior and multi-scale retinex," in *Proc. Int. Conf. Intell. Syst. Design Eng. Appl.*, vol. 1, Oct. 2010, pp. 848–851.
[39] J.-P. Tarel, N. Hautiere, A. Cord, D. Gruyer, and H. Halmaoui, "Improved visibility of road scene images under heterogeneous fog," in *Proc. IEEE Intell. Vehicles Symp.*, San Diego, CA, USA, Jun. 2010, pp. 478–485. [Online]. Available: http://perso.lcpc.fr/tarel.jean-philippe/publis/iv10.html
[40] A. Gaidon, Q. Wang, Y. Cabon, and E. Vig, "Virtual worlds as proxy for multi-object tracking analysis," in *Proc. CVPR*, Jun. 2016, pp. 4340–4349.
[41] C. O. Ancuti, C. Ancuti, R. Timofte, and C. De Vleeschouwer, "O-HAZE: A dehazing benchmark with real hazy and haze-free outdoor images," in *Proc. IEEE/CVF Conf. Comput. Vis. Pattern Recognit. Workshops (CVPRW)*, Jun. 2018, pp. 754–762.
[42] B. Li, W. Ren, D. Fu, D. Tao, D. Feng, W. Zeng, and Z. Wang, "Benchmarking single-image dehazing and beyond," *IEEE Trans. Image Process.*, vol. 28, no. 1, pp. 492–505, Jan. 2019.
[43] A. Galdran, "Image dehazing by artificial multiple-exposure image fusion," *Signal Process.*, vol. 149, pp. 135–147, Aug. 2018.
[44] H. Kong, J.-Y. Audibert, and J. Ponce, "Vanishing point detection for road detection," in *Proc. IEEE Conf. Comput. Vis. Pattern Recognit.*, Jun. 2009, pp. 96–103.
[45] R. Grompone Von Gioi, J. Jakubowicz, J.-M. Morel, and G. Randall, "LSD: A line segment detector," *Image Process. Line*, vol. 2, pp. 35–55, Mar. 2012.
[46] Z. Wang, A. C. Bovik, H. R. Sheikh, and E. P. Simoncelli, "Image quality assessment: From error visibility to structural similarity," *IEEE Trans. Image Process.*, vol. 13, no. 4, pp. 600–612, Apr. 2004.
[47] N. Hautière, J.-P. Tarel, D. Aubert, and É. Dumont, "Blind contrast enhancement assessment by gradient ratioing at visible edges," *Image Anal. Stereol. J.*, vol. 27, no. 2, pp. 87–95, Jun. 2008.
[48] A. Mittal, R. Soundararajan, and A. C. Bovik, "Making a 'completely blind' image quality analyzer," *IEEE Signal Process. Lett.*, vol. 20, no. 3, pp. 209–212, Mar. 2013.
[49] X. Min, G. Zhai, K. Gu, X. Yang, and X. Guan, "Objective quality evaluation of dehazed images," *IEEE Trans. Intell. Transp. Syst.*, vol. 20, no. 8, pp. 2879–2892, Aug. 2019.

MINSUB KIM received the B.S. degree in electronics engineering from Yonsei University, Seoul, South Korea, in 2014, where he is currently pursuing the Ph.D. degree with the Department of Electrical and Electronic Engineering.

His current research interests include dehazing, resolution improvement for ADAS, contrast enhancement, and image quality assessment based on the human visual systems.

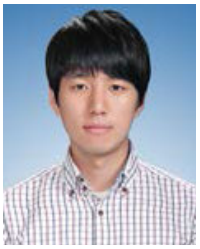

SOONYOUNG HONG received the B.S. degree in electronic engineering from Yonsei University, Republic of Korea, in 2015, where he is currently pursuing the Joint M.S. and Ph.D. degrees with the Department of Electrical and Electronic Engineering.

His current research interests include contrast enhancement, dehazing, and high dynamic range.

HAEGEUN LEE received the B.S. degree in electrical and electronic engineering from Yonsei University, South Korea, in 2016, where he is currently pursuing the Ph.D. degree with the School of Electrical and Electronic Engineering.

His current research interests include superresolution image processing and image restoration.

MOON GI KANG received the B.S. and M.S. degrees in electronics engineering from Seoul National University, Seoul, South Korea, in 1986 and 1988, respectively, and the Ph.D. degree in electrical engineering from Northwestern University, Evanston, IL, USA, in 1994.

From 1994 to 1997, he was an Assistant Professor with the University of Minnesota, Duluth, MN, USA. Since 1997, he has been with the Department of Electronic Engineering, Yonsei University, Seoul, where he is currently a Professor. He has authored more than 100 Technical articles in his areas of expertise. His current research interests include image and video filtering, restoration, enhancement, and superresolution reconstruction. He was a recipient of the 2006, 2007, and 2012 Yonsei Outstanding Research Achievement awards (Technology Transfer), the 2002 HaeDong Foundation Best Paper Award, and the 2000, 2009, and 2010 awards of Teaching Excellence at Yonsei University. He has served in the technical program and steering committees of several international conferences. He served as an Editorial Board Member for the *IEEE Signal Processing Magazine*, an Editor of SPIE Milestone Series Volume (CCD and CMOS imagers), and a Guest Editor of the *IEEE Signal Processing Magazine* Special Issue on Superresolution Image Reconstruction, in May 2003. He has also served as an Associate Editor of the *EURASIP Journal of Advances in Signal Processing* and an Associate Editor of the *Digital Signal Processing* in Elsevier Journal.